

Pore structure analysis of particle beds for fluid transport simulation during filtration

C.L. Lin, J.D. Miller*

Department of Metallurgical Engineering, College of Mines and Earth Sciences, University of Utah, 135 South 1460 East, Room 412, William C. Browning Building, Salt Lake City, UT 84112, USA

Received 11 October 2002; received in revised form 10 March 2003; accepted 2 May 2003

Abstract

Accurate assessment of the transport properties of porous media (in our case, filter cake) is of major importance in the development of improved filtration processes. Implications from these studies are important in the design and operation of filtration equipment in order to enhance the efficiency of this important solid–liquid separation process. The microstructure and connectivity of pore space are important features to describe detailed fluid flow phenomena in filter cake during fine particle filtration. In this regard, 3D characterization of pore structure is essential. The pore structure has to be described by parameters which are of special relevance to the interpretation of fluid transport phenomena. These parameters should be based on directly measured variables of the pore system and not inferred from indirect variables (such as those determined empirically from transport processes) valid only for a particular pore structure. In this way, fundamental relationships between pore structure and fluid transport at the microstructure level can be described. In order to achieve this level of sophistication, the three-dimensional interconnected pore structure of filter cake must be determined.

Study of fluid transport phenomena in filter cake using X-ray microtomography (XMT) to characterize the complex three-dimensional pore geometry is discussed. On this basis, the lattice Boltzmann (LB) method is used to simulate fluid flow and to begin to establish a fundamental relationship between pore microstructure and effective transport coefficients. For example, can network analysis using skeletonization procedures be used to confirm fundamental relationships that might be developed? Eventually then, with this detailed model, design and operating variables could be optimized for improved filtration efficiency. © 2004 Elsevier B.V. All rights reserved.

Keywords: filtration; fluid flow; transport simulation; porous media; lattice Boltzmann method; X-ray microtomography

1. Introduction

Filtration processes are widely used in different industrial applications including water treatment and

reclamation, water purification for the pharmaceutical, micro-electronic, chemical and mineral industries, separation of hazardous solids from chemical wastes and removal of deleterious components from paper pulp. Filtration of fine particles involves filter cake formation and removal of surface moisture by drawing air through the porous structure. Typically, the phrase “fluid flow in porous media” is commonly used to describe this phenomena. Porous media can be

* Corresponding author. Tel.: +1-801-581-5160; fax: +1-801-581-4937.

E-mail address: cllin.jdmiller@mines.utah.edu (J.D. Miller).

considered as a mixture of solid and pore frameworks. It is known that macroscopic flow properties are related to microscopic (pore level) properties. In this regard, the geometry, both the microstructure and the connectivity of pore space, plays a fundamental role in governing fluid transport through porous media. This is especially true for single-phase, incompressible flow where the dominant flow factor is the fluid-wall surface tension. In general, the macroscopic quantity of interest is more or less influenced by the microscopic properties of the structure and the connectivity of pore space and is obtained by a spatial integration of the local field. Most efforts for detailed model development are to establish the relationship between the geometrical properties of the pore microstructure and the bulk flow properties of the media. Direct measurement of the pore space and random nature of its microstructure are the major obstacles for model development.

Before the 1980s, most of the porous media models focussed on the bulk average quantities such as porosity, specific surface area and tortuosity; however, due to the random nature of the pore space, geometric descriptive parameters need to be established to understand the complex, random spatial distributions of porous media and the correlation between parameters. The n -point covariance functions (Quiblier, 1984; Berryman and Blair, 1986; Adler et al., 1990; Torquato, 1991; Coker et al., 1996) play an important role in this characterization. Artificial samples can be reconstructed based on the measurements of the two-point covariance function from digitized images of rocks (Adler et al., 1990; Thovert et al., 1993; Yao et al., 1993). Further, the properties of these reconstructed rocks have been studied. Such correlation functions have been useful analytical tools in the theoretical description of porous media. However, for accurate fluid flow study, it is important to note that it is incorrect to study 3D flow properties using parameters obtained from 2D images because the connectivity in three dimensions and two dimensions are fundamentally different. Since the connectivity of the pore space has a critical influence on transport properties such as permeability (Martys et al., 1994), its quantification can be critical for proper understanding of microstructure–transport property relationships.

Until the 1990s, most direct measuring methods used to characterize the pore microstructure and the connectivity relied on the microscopic observation of a series of thin sections or polished sections of the porous media (Dullien, 1992; Lymberopoulos and Payatakes, 1992). These data sets were then used to reconstruct and to display the 3D image of the porous system with the help of advanced computer graphic techniques. The disadvantages of this serial section method are obvious and include tedious and time-intensive processes (mounting, polishing, slicing and digitization), destruction of the samples, and non-isotropic spatial resolution (usually better lateral resolution than axial resolution). As the resolution and the techniques for 3D geometric analysis have advanced in the last decade, it is now possible to map in detail the pore structure in three-dimensional digital space nondestructively using high-resolution X-ray microtomography (XMT) to describe features with micrometer resolution.

2. Simulation of fluid flow through porous media

Besides the characterization of pore structure for completely interconnected filter cake structures, an understanding of how flow transport properties, such as permeability, depend on pore microstructure is of significance. Various approaches based on experimental, theoretical, and computer simulation methods have been applied to study flow phenomena in porous media. Details of these models have been reviewed and are discussed in the literatures (Dullien, 1992; Bryant et al., 1993; Sahimi, 1995). Both network models (Bryant et al., 1993; Celia et al., 1995) and lattice Boltzmann (LB) methods (Frisch et al., 1986; Rothman and Zaleski, 1997; Chopard and Droz, 1998; Wolf-Gladrow, 2000) provide a means of numerically studying relationships between microscopic geometry of pore space and bulk flow properties.

2.1. Network model

Capillary network models, one of the pore structure models, has been used to mimic porous media. For capillary networks, the pore structure is modeled by arrays of capillary tubes. The pore structure of filter cake can be thought to consist of an interconnected

three-dimensional network of voids, pores or capillaries. This three-dimensional network usually has irregular geometry, with different shapes and sizes of capillary segments distributed over the network in irregular fashion. A schematic network model for a complex pore structure is shown in Fig. 1. The important parameters for estimation of the transport properties are the medial axis (or skeleton) of the interconnected pore system, throat diameters along the skeleton, length of the pore throat and nodal pore size.

Originally, skeletonization (Blum, 1967) (in a plane) denoted a process which transforms a 2D object into a 1D graph-like structure, comparable to a stick figure. It is thereby essential that the skeleton retains the original connectivity of the shape. Unfortunately, for 3D objects, there are two different types of skeleton: the medial surface and the medial axis. For instance, the medial surface will be generated using a 3D skeletonization process for non-isometric channel. Of course, for isometric channels, 3D skeletonization results in a medial axis. Now the skeletonization process provides both the radius information and structure of the object space. This information of 3D interconnected pore space provides a tool to describe important properties of the completed pore

structure and can be used for the capillary network simulation by percolation theory. Several approaches such as topological thinning (Tsao and Fu, 1981; Gong and Bertrand, 1990; Lee et al., 1994; Ma and Sonka, 1996), distance transformation (DT) (Borgefors, 1984; Gagvani and Silver, 1997), discrete Voronoi skeletons (DVS) (Ogniewicz and Ilg, 1992) and the marching core method (Furst et al., 1996) can be used for algorithm development of the 3D skeletonization process. The corresponding length and radius of the skeleton segments from the network graph can be used as attributes of the capillary tubes for the 3D interconnected pore structure. Furthermore, this information can be used to more accurately represent probabilities for the capillary network simulation using percolation theory.

2.2. Lattice Boltzmann method

During the last decade, rapid development of computers and computational algorithms has made possible direct simulations of complicated fluid flow phenomena. Among the promising new methods are lattice-gas automata (LGA) and lattice Boltzmann (LB) methods that can be applied to a large variety of fluid flow problems. The geometrical versatility of these methods makes them particularly useful in simulating flows in irregular geometries (Qian et al., 1992; Gunstensen and Rothman, 1993; Succi et al., 1995; Noble et al., 1995; Martys and Chen, 1996; Chen and Doolen, 1998; Ferreol and Rothman, 1995; Koponen et al., 1997; Dardis and McCloskey, 1998; Bosl et al., 1998; Stockman et al., 1997, 1998). Within this numerical approach, various macroscopic parameters of flow, such as permeability and tortuosity, and parameters of pore structure, such as porosity and specific surface area, can be correlated. A brief description of the LB method is provided as follows.

First, in the LGA method, a discrete set of fluid particles moves in a discrete space (lattice) in discrete time. The particles undergo collisions at the lattice nodes according to a certain set of collision rules. These collision rules are set in a way that conserves mass (i.e. particle number) and momentum. The microscopic dynamics of such a model of a fluid are simple, but the macroscopic dynamics contain essentially the same complexity as hydrodynamics itself. Momentum and particle averages for single-phase

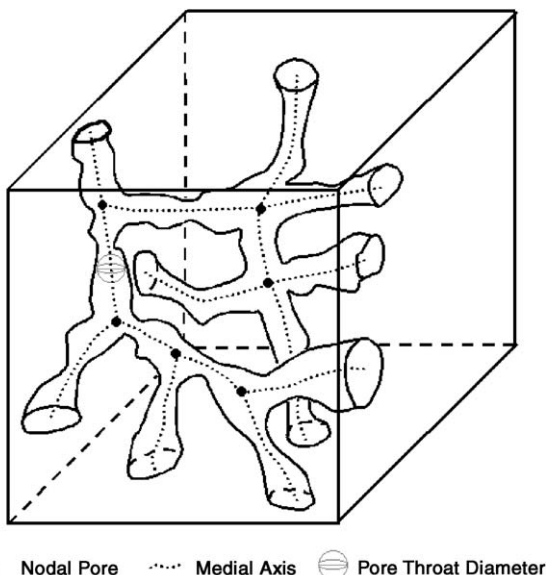


Fig. 1. Schematic representation of the interconnected pore system and characteristic parameters used to estimate transport properties by the network model.

LGA models, taken over many sites or many time steps, obey the equations:

$$\nabla \cdot \vec{u} = 0 \quad (1)$$

$$\frac{\partial \vec{u}}{\partial t} = -\frac{\nabla p}{\rho} - g(\rho) \cdot (\vec{u} \nabla) \vec{u} + \nu \cdot \nabla^2 \vec{u} + \vec{F} \quad (2)$$

where t is time, \vec{u} is the fluid velocity, p is the pressure, ν is the kinematic viscosity, ρ is the density in particle/site and \vec{F} is the body force (e.g. gravity). Eq. (1) arises from the conservation of mass in the lattice gas and Eq. (2) derives from the conservation of momentum. Eq. (2) is very similar to the Navier–Stokes equation. For steady-state flow, the $g(\rho)$ term can be absorbed into the viscosity, pressure and force terms, making Eq. (2) effectively equivalent to Navier–Stokes.

The LB method is a probabilistic equivalent of the LGA method, where the discrete fluid particles are replaced with the respective values of their mean population. The LB method circumvents two major shortcomings of the LGA method: intrinsic noise and limited values of transport coefficients, both due to the Boolean nature of the LGA method. For application of flow through porous media, the LB method is easier to implement in 3D. The LB methods with a simple BGK collision operator (Qian et al., 1992), known as the ‘relaxation-Boltzmann’ scheme, is written:

$$f_i(\vec{x} + \vec{e}_i, t + 1) = f_i(\vec{x}, t) - \frac{(f_i(\vec{x}, t) - f_i^{\text{eq}}(\vec{x}, t))}{\tau} \quad (3)$$

where f_i represent the particle distribution functions for each vector direction i , t is time, \vec{x} is the (x, y, z) position in the lattice, \vec{e}_i is the velocity in the i th direction, f_i^{eq} is the equilibrium particle distribution, and τ is the relaxation parameter. The left side of the equation is analogous to the “translation” stage in LGA method, and the right side to the “collision” stage.

This paper presents the study of fluid transport phenomena in filter cake using X-ray microtomography to characterize the complex three-dimensional pore geometry. On this basis, the Lattice Boltzmann (LB) method is used to simulate and to establish a

fundamental relationship between pore microstructure and effective transport coefficients. In this regard, 3D digital maps of samples obtained from both the simulated cake (packed bed of spherical particles) and the irregular interconnected pore structure of actual particle beds obtained from X-ray microtomography (XMT) analysis are studied using the lattice Boltzmann method for flow simulation.

3. Lattice Boltzmann simulation of flow in packed beds

The classical approach (Tiller, 1975; Dahlstrom and Silverblatt, 1977; Svarovsky, 1990) for filtration analysis is based on Darcy’s law, an empirical equation that describes one-dimensional fluid flow through a uniform incompressible porous media. Knowledge of cake pore microstructure and its correlation to macroscopic cake properties is required to model the filtration from a fundamental point of view. Darcy’s law is defined as

$$U = \frac{Q}{A} = \frac{1}{A} \frac{dV}{dt} = \frac{k \Delta p}{\mu \ell} \quad (4)$$

where U is the fluid velocity, Q is the volume flow rate, V is the volume of the fluid, k is the permeability,

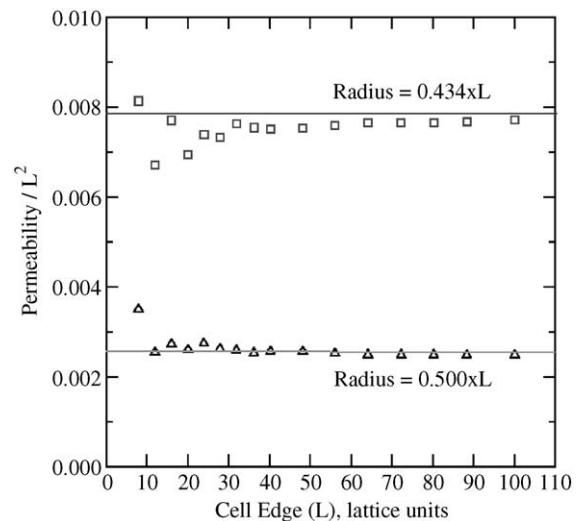


Fig. 2. LB estimate of permeability of simple cubic array of sphere, as function of cell edge (L) (Stockman, 2001). The values from Zick and Homsy (1982) are shown as solid lines.

Table 1

Size distribution by weight, number of spheres calculated for each size interval, and values of α and dc , for simulation of samples A and B

Sample	Average size (μm)	Weight percent	Number of spheres
A ($\alpha=0.99$ and $dc=35$)	127	2.77	3
	90	5.08	16
	63	8.94	81
	48	8.83	181
	41	5.60	184
	31	10.20	777
	22	12.02	2561
	16	46.56	25 786
B ($\alpha=2.18$ and $dc=57$)	111	6.66	11
	63	22.15	201
	48	21.46	440
	41	11.14	367
	34	10.91	630
	26	11.16	1441
	19	7.81	2583
	14	8.71	7201

μ the viscosity of the fluid, A the cross-sectional area of the one dimensional sample of length (or thickness of porous media) ℓ and Δp is the pressure drop.

Presently, LB models are used as common tools to study transport phenomena through pore space (Noble et al., 1995; Ferreol and Rothman, 1995; Koponen et al., 1997; Dardis and McCloskey, 1998; Bosl et al., 1998; Stockman, 1999). For this study, permeability was computed by modeling Stokes flow in both the

simulated pore space of a packed bed and actual 3D digital pore space from X-ray microtomography (XMT) analysis using the LB method. The particular model used for this study is the one developed by Stockman (1999). Details of this model can be found in the literature (Stockman, 1999). Only the issue regarding the calculation of permeability is summarized here as follows.

The permeability of a simple cubic array of spheres, at low Re is well known (Zick and Homsy, 1982) and provides a basic benchmark for testing the accuracy of LB models for single-component flow in porous media. For non-overlapped spheres, the per-

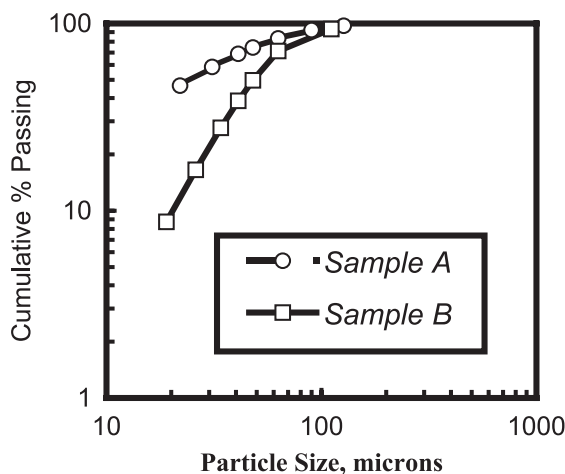


Fig. 3. Particle size distributions of samples A and B used for LB simulations.

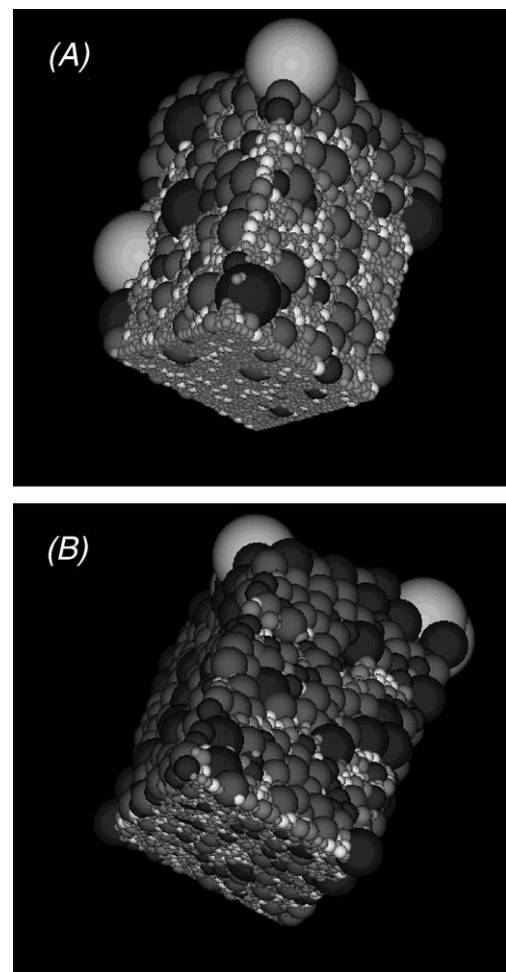


Fig. 4. Three-dimensional images of simulated packed beds of samples A and B.

meability k (unit of length²) is related to the drag coefficient C_d ,

$$k = \frac{v}{6\pi R C_d} \quad (5)$$

where v is the unit cell volume and R is the sphere radius. For Darcy flow,

$$k = -\frac{U\mu}{dP/dx} \quad (6)$$

Compared with Eq. (4), U is the fluid velocity, average across an inlet or outlet face of the unit cell (including solids), μ is the dynamic viscosity, and dP/dx is the pressure gradient along the x -direction. Formally, the LB used in this study is a constant-pressure model, so the pressure gradient must be related to the body force. To relate the permeability to units measured in the LB simulation, a force balance was applied:

$$xBody\rho L^3 = (P_{in} - P_{out})L^2 = -(dP/dx)L^3 \quad (7)$$

or $(dP/dx) = -xBody\rho$, where L is the side of the simulation cell (in lattice units), $xBody$ is the body force, applied in the x -direction, per unit volume in the LB simulation, and ρ is the particle density per site specified in the LB simulation. Thus

$$k = \frac{Uv}{xBody} \quad (8)$$

where $v = \mu/\rho = (\tau - 1/2)/3$ is the kinematic viscosity specified in the LB simulation as shown in Eq. (4).

Customarily k/L^2 , normalized permeability, is reported rather than k , to achieve scale independence.

4. Results

4.1. Accuracy of LB flow simulation

First, we check the accuracy of the LB model for this study by examining the estimated permeability of a simple cubic array of spheres (Stockman, 1999) and compare this estimation with the permeability value given by Zick and Homsy (1982). In Fig. 2, the apparent k/L^2 value, measured in the LB simulation, is plotted as a function of cell edge (L). The error in the estimated permeability drops from $\sim 15\%$ at $L=8$, to $\sim 1\%$ at $L>30$. Most of the error at low L can be attributed to pixelation effects (Stockman, 1999). It is evident that the LB model can give a good estimate of permeability.

4.2. LB flow through simulated packed particle beds

The sets of pore space we consider are associated with the packing of spherical particles (Lin and Miller, 2000). In the packed stage, spheres (from a specified size distribution) are dropped into box by Monte Carlo simulation. This algorithm (Lin and Miller, 2000) generates high-porosity, unconsolidated, three-dimensional packing structures usually referred to as random-loose packing. Two samples are

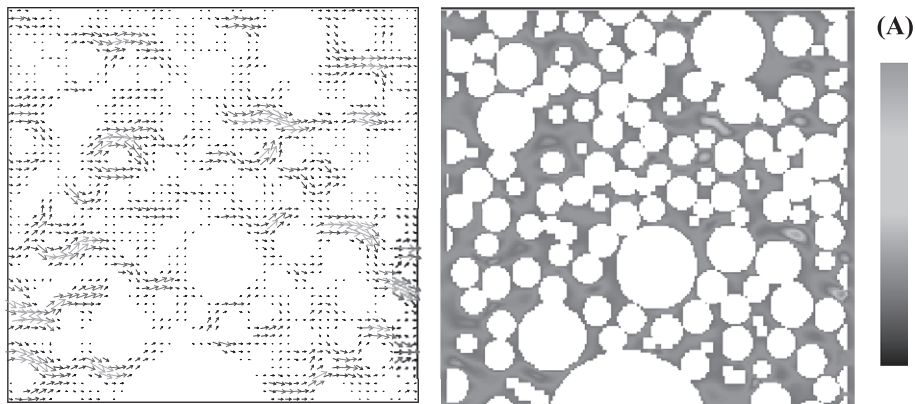


Fig. 5. Velocity and vector plots of LB simulation for flow through simulated pore space of packed particle bed (middle section of sample A).

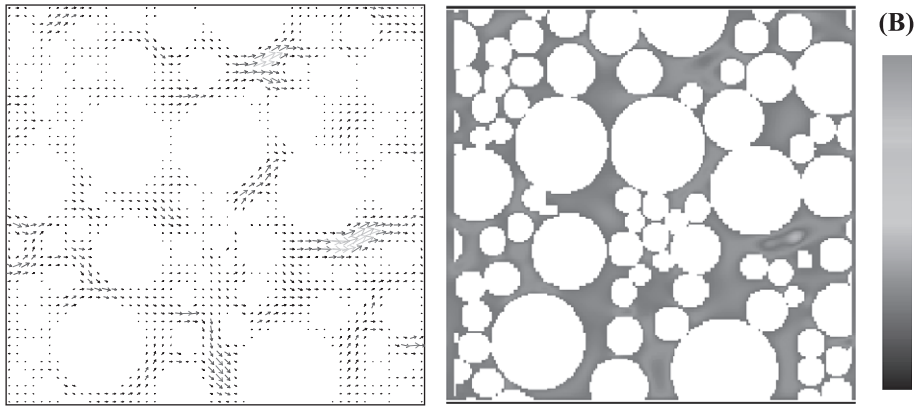


Fig. 6. Velocity and vector plots of LB simulation for flowthrough simulated pore space of packed particle bed (middle section of sample B).

considered for this study. Table 1 shows the size distributions, the number of particles considered for each size interval, the values of α (dispersion constant) and dc (absolute size constant). The number of particles was obtained from the weight of particles in each size interval (total weight $\sim 5.0 \times 10^{-4}$ g) using particle density (~ 4.90 g/cm³) and size. Particle size distributions for samples A and B are plotted and shown in Fig. 3. The 3D images of the simulated cake after 10000 cycles are shown in Fig. 4.

Only the interior $200 \times 100 \times 200$ blocks, from height at 10 pixels (or 50 μm) located above the center, are sectioned and used for the calculation of

permeability, k , by LB simulation. For LB simulation, these block samples were constrained at the left and right with the top and bottom boundaries open. The body force was applied from top-to-bottom. Figs. 5 and 6 illustrate the velocity and vector plots of the middle slice of the packed particle bed for samples A and B, respectively. The velocity scale, for all figures presented in this paper is gray-coded as shown by the gray scale bars. Solids are white, and the solution velocity ranges from black for no flow, through decreasing gray levels for higher velocity. Flow direction is from left to right. Fig. 7 shows the comparison of the steady state velocity profile from four slices of the packed particle bed for

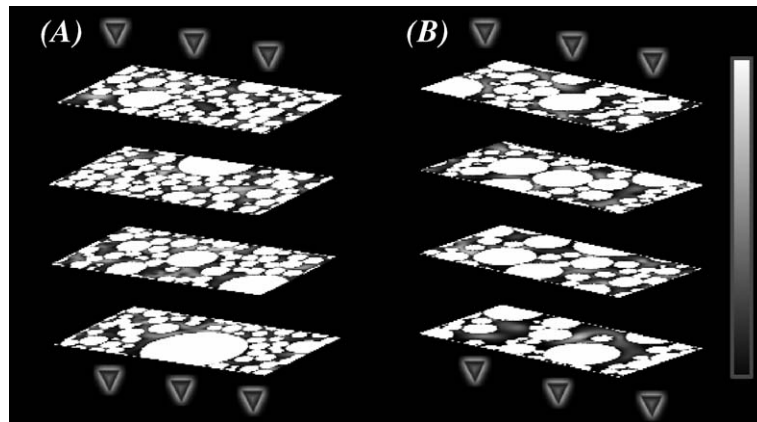


Fig. 7. LB simulated fluid velocity variations through packed beds of spheres, samples A and B. Solids are white, and the solution velocity ranges from black for no flow, through decreasing gray levels for higher velocity.

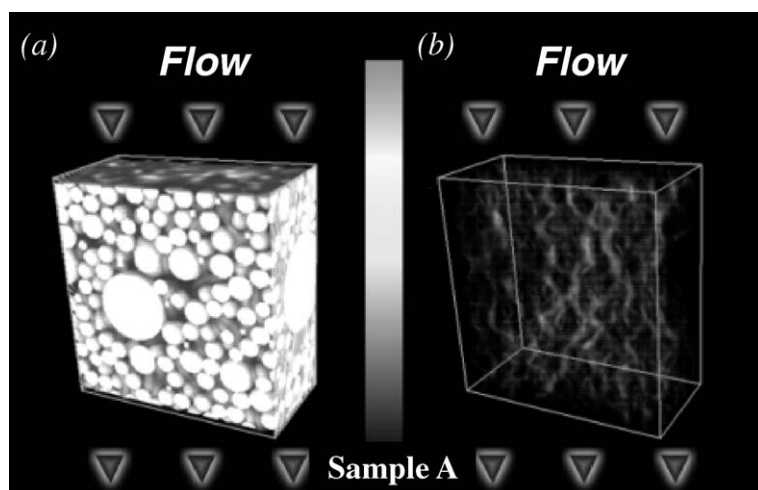


Fig. 8. 3D views of LB simulated flow through a packed bed of spheres, sample A: (a) with solid phase as white and (b) with transparent phase. The gray bar shows that the solution velocity ranges from black for no flow, through decreasing gray levels for higher velocity.

samples A and B. The gray scale used for this figure illustrates the fluid velocity magnitude and light gray is the maximum velocity. White designates the solid phase.

Figs. 8 and 9 illustrate the 3D view of the LB simulated flow through the pore space of packed beds of spheres, samples A and B, respectively. Once we remove the solid particle phase, Figs. 8b and 9b show

the nature of the flow channels. The main thing to notice is that most of the flow occurs in a small fraction of the available pore space.

As mentioned previously, connectivity plays an important role in the distribution of flow inside porous media. It seems that several main channels carry almost all the flow. This can be attributed to the flow becoming increasingly controlled by narrow pore

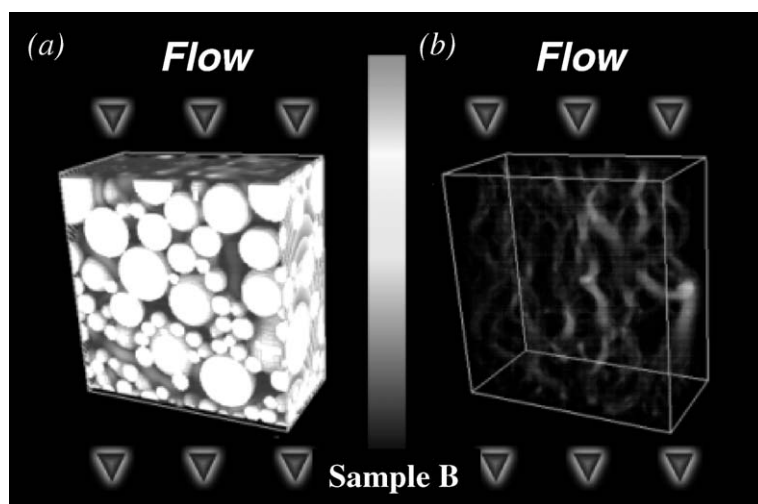


Fig. 9. 3D views of LB simulated flow through a packed bed of spheres, sample A: (a) with solid phase as white and (b) with transparent phase. The gray bar shows that the solution velocity ranges from black for no flow, through decreasing gray levels for higher velocity.

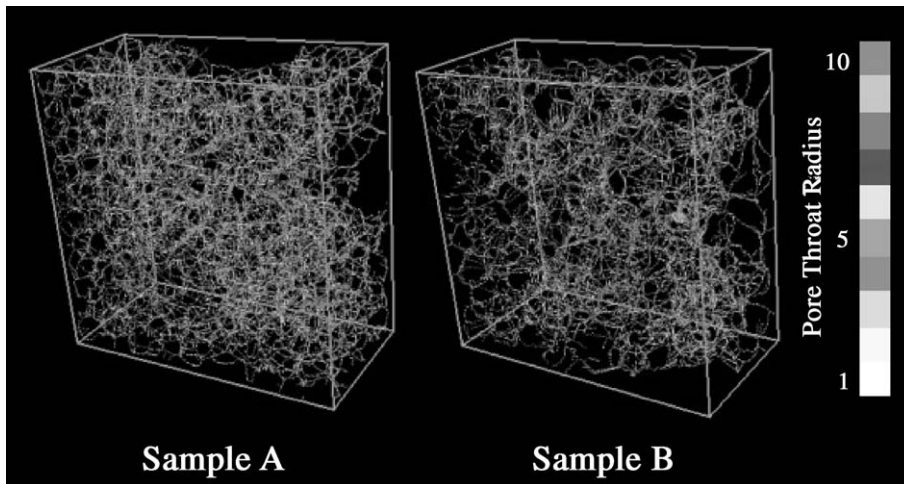


Fig. 10. Network of the skeleton segments and their corresponding pore throat radii for samples A and B.

throats, so that the fluid picks out a continuous path connected by the largest pore throat sizes. In this regard, a 3D skeletonization process (Lee et al., 1994; Borgefors, 1984; Lin and Miller, 2000) was performed for the 3D interconnected pore structures of samples A and B. The network of the skeleton segments and their corresponding radii for samples A and B are shown in Fig. 10.

Fig. 11 shows the normalized velocity distribution from LB simulation for samples A and B. The major features of the normalized velocity distribution is the sharp peak near velocity = 0, after that the normalized velocity distribution decays smoothly with increase in velocity. The nearly singular behavior near velocity = 0 can be explained due to the fact that most near-zero flow occurs near the spherical particle surface, which dominates the geometry (Maier et al., 1998). To illustrate the effect of geometry pore microstructure on the normalized velocity distribution, the distributions of pore-throat radius along the 3D skeleton network graph of pore space were normalized and plotted in Fig. 12. Comparison between normalized velocity and pore throat radius distribution indicates the qualitative agreement between these two distributions.

The main object of this study is to establish the relationship between the geometrical properties of the pore microstructure and the bulk flow properties of the media. In this regard, permeabilities are estimated

from LB simulations of flow through the packed beds (samples A and B). As mentioned previously, the estimated permeabilities from LB simulations are normalized by the mean sphere diameter. This is the only way to compare permeability values between granular materials with different pore scales. Fig. 13 illustrates the estimated normalized perme-

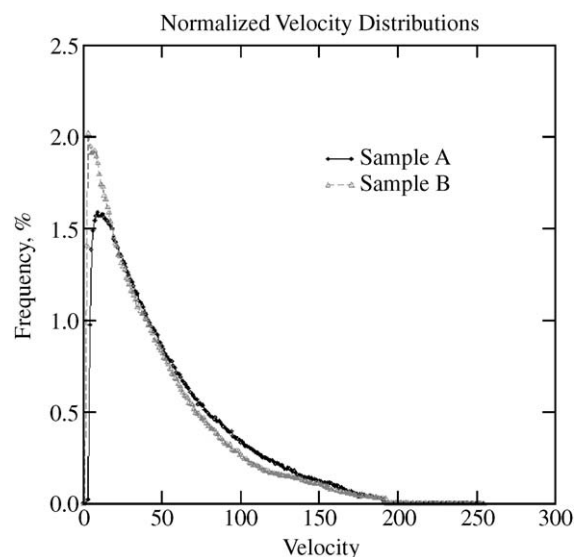


Fig. 11. Normalized velocity distribution for LB simulation of packed beds of spheres.

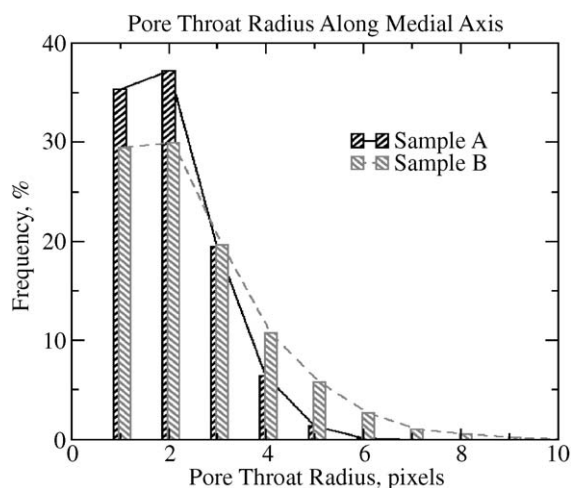


Fig. 12. Normalized pore throat radius along the skeleton segments of the pore space network.

ability, k/d^2 , of samples A and B. Also included in the figure are the permeability values calculated based on the uniform expansion and random-fill models (Bosl et al., 1998). A good agreement was observed between our computed permeability values and the values reported in the literature (Bosl et al., 1998).

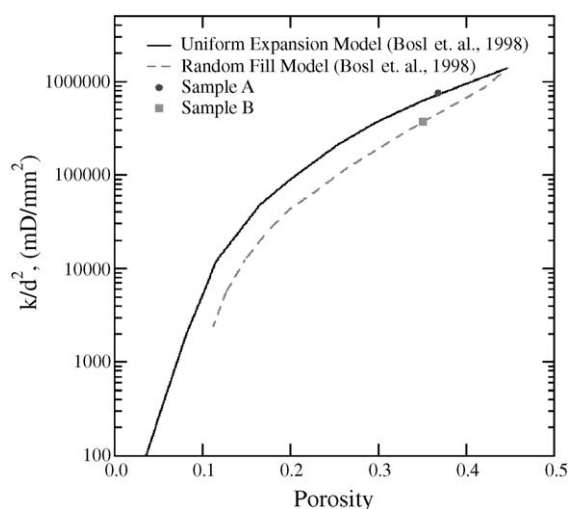


Fig. 13. Estimated permeability and porosity for samples A and B obtained from LB simulations. Porosity–permeability curves for uniform sphere expansion and random filling models (Bosl et al., 1998) are plotted for comparison.

4.3. LB flow through tomographically reconstructed packed particle beds

The microstructure and the connectivity of pore space are important to describe fluid flow in filter cake during fine particle filtration. In this regard, characterization of pore structure based on parameters permitting inferences on the fluid balance is of particular interest. The pore structure has to be described by parameters which are of special relevance for the interpretation of fluid transport phenomena. These parameters should be based on directly measured variables of the pore system and

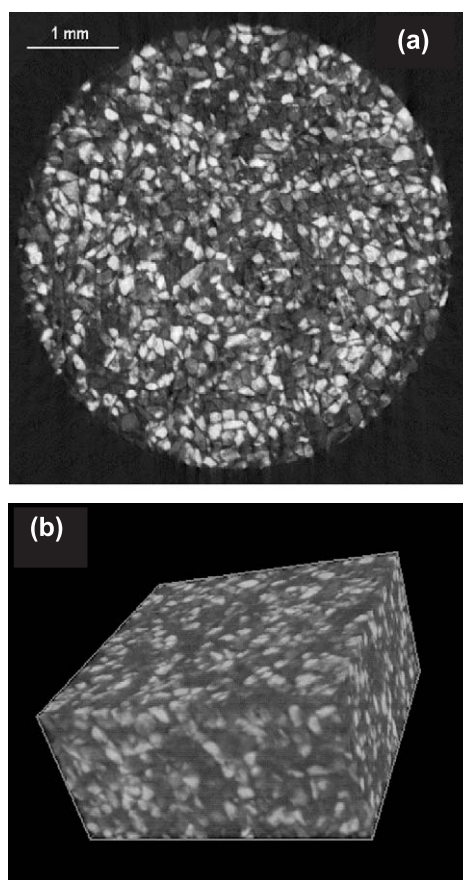


Fig. 14. Structure of the bed of iron ore particles obtained with the new cone beam X-ray microtomography system at the University of Utah. (a) Selected cross-sectional image from a packed bed of iron ore particles ($180 \times 106 \mu\text{m}$). (b) Volume-rendering image from a subset ($256 \times 256 \times 128$) of the packed bed of iron ore particles.

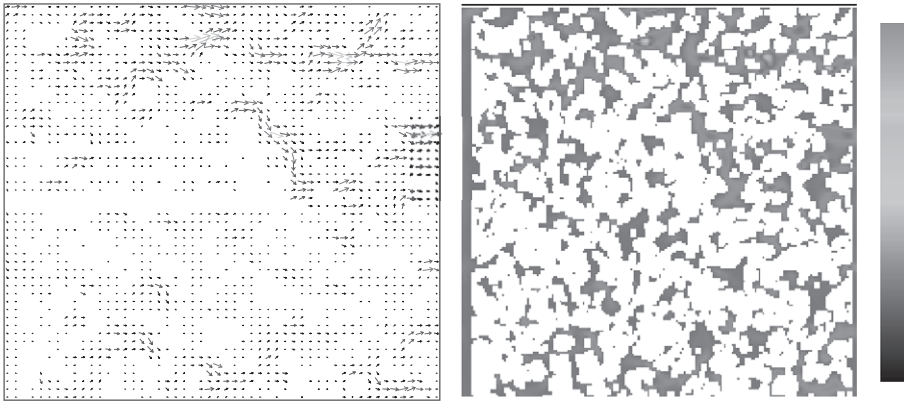


Fig. 15. Velocity and vector plots of LB simulation for flow left to right through tomographically reconstructed images of a packed particle bed (sample C, porosity 0.302).

not indirect variables (such as those determined empirically from transport processes) valid only for a particular pore structure. In this way, fundamental relationships between pore structure and fluid transport at the microstructure level can be described. Thus, it is desired to be able to directly measure the three-dimensional interconnected pore structure of filter cake.

Two 3D reconstructed images of complex filter cake pore structure obtained from high-resolution 3D X-ray microtomography measurement were used for

this study. The voxel size for the first set of data, namely sample C, for a packed bed (with particle size of $210 \times 150 \mu\text{m}$) is $17 \mu\text{m}$. Details procedures and characteristics of the first sample can be found in our previous pore geometry study (Lin and Miller, 2000). The second set of data (sample D), a packed bed of iron ore particles ($180 \times 106 \mu\text{m}$), was prepared and scanned using the newly installed cone beam X-ray microtomography system (Lin and Miller, 2001). Fig. 14a shows one slice from the volume data set for the packed bed of iron ore particles. A volume-rendering

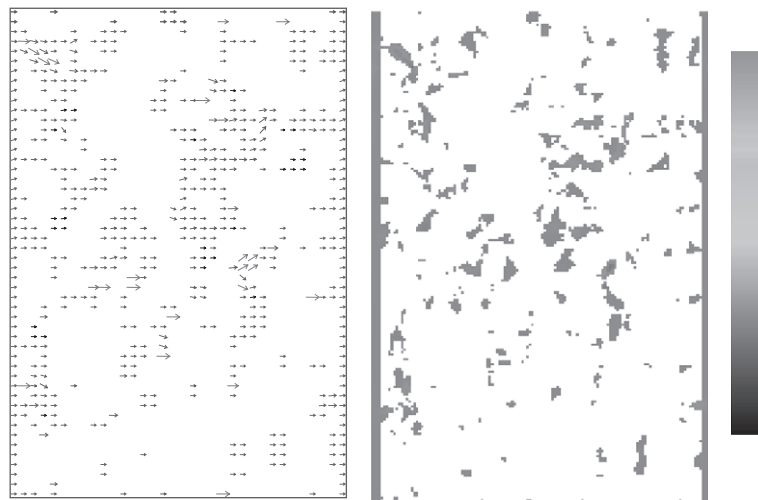


Fig. 16. Velocity and vector plots of LB simulation for flow left to right through tomographically reconstructed images of a packed particle bed (sample D, porosity 0.0673).

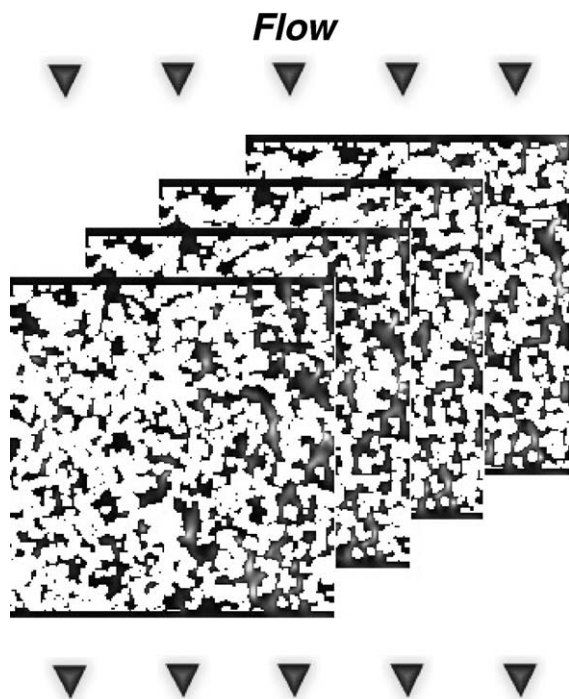


Fig. 17. LB simulation of velocity variations through tomographically reconstructed images of a packed particle bed (sample C).

image from a subset of this sample ($256 \times 256 \times 128$) is shown in Fig. 14b. The voxel size for this sample is $10 \mu\text{m}$. Considerable improvement in resolution was achieved with our newly installed X-ray microtomography (XMT) system which is better than the system used in the previous study.

To illustrate the feasibility of the lattice Boltzmann (LB) simulation for fluid flow through a packed bed of particles, simulation was done using a reconstructed 3D data set obtained by XMT (Lin and Miller, 2000). Block sizes of $200 \times 100 \times 200$ (sample C, porosity 0.302) and $200 \times 200 \times 128$ (sample D, porosity 0.0673) from the 3D reconstructed images were constrained at the left and right with the top and bottom boundaries open. The procedure for LB simulation is identical as mentioned previously. Figs. 15 and 16 show the velocity and vector plots of one slice of the packed particle bed for samples C and D, respectively.

Fig. 17 shows the steady state velocity profile through sample C from four adjacent slices of the packed particle bed for uniform distribution of solution. 3D views of LB simulated flow through the 3D reconstructed pore space of packed particle beds, samples C and D, are shown in Figs. 18 and 19, respectively. Once we remove the solid particle phase,

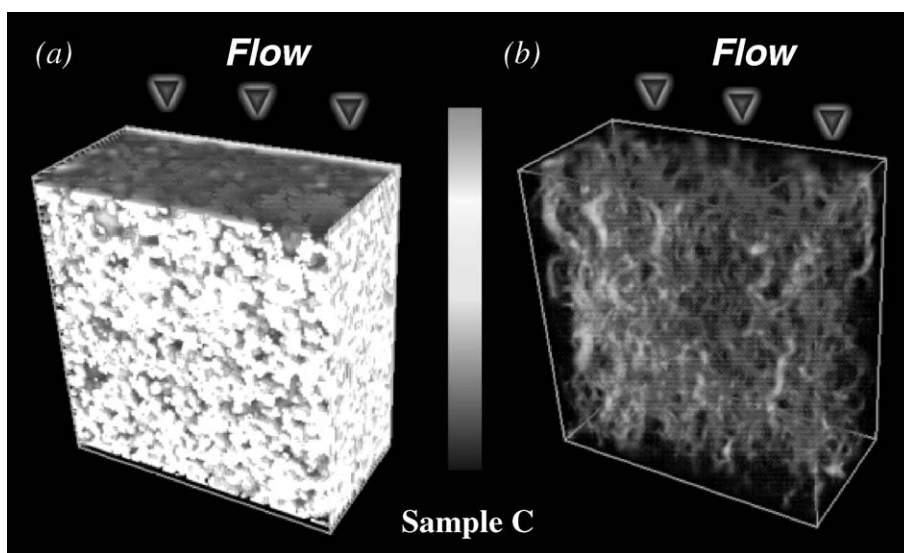


Fig. 18. 3D views of LB simulated flow through a packed particle bed for sample C: (a) with solid phase as white and (b) with transparent solid phase.

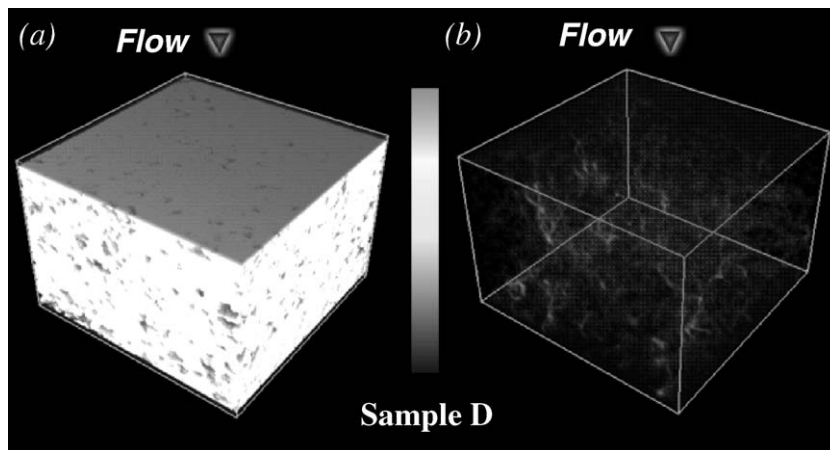


Fig. 19. 3D views of LB simulated flow through a packed particle bed for sample D: (a) with solid phase as white and (b) with transparent solid phase.

Figs. 18B and 19B show the nature of the flow channels. The main thing to notice is that most of the flow occurs in a small fraction of the available pore space. The estimated permeabilities for samples C and D are 4.02×10^{-7} and $7.77 \times 10^{-8} \text{ cm}^2$, respectively.

5. Summary

In order to gain a better understanding of the complex transport phenomena that occur in a filter cake, study of the effect of three-dimensional pore geometry on the effective transport properties of the filter cake is necessary. Transport calculations have been carried out for both simulated and actual three-dimensional porous media (in our case, filter cake) using the lattice Boltzmann method. Accuracy of the estimated permeabilities from LB simulations were checked and compared with results found in the literature. Results indicate that good quantitative agreement can be achieved for flow simulation through complex porous media using the LB method.

Velocity distribution profiles obtained from LB simulations indicate that most of the flow occurs through major flow channels which have the distribution of large pore throat diameters. A 3D skeletonization process was performed to confirm the observation of major flow channels. Quantitative correlation be-

tween the major flow channel and network skeleton of pore space is in progress.

Acknowledgements

The authors would like to thank Dr. Harlan W. Stockman, Sandia Laboratory, for help with the lattice Boltzmann simulation.

References

- Adler, P.M., Jacquin, C.J., Quiblier, J.A., 1990. Flow in simulated porous media. *Int. J. Multiph. Flow*. 16, 691–712.
- Berryman, J.G., Blair, S.C., 1986. Use of digital image analysis to estimate fluid permeability of porous materials: application of two-point correlation function. *J. Appl. Phys.* 60, 1930–1938.
- Blum, H., 1967. A transformation for extracting new descriptors of shape. *Models for the Perception of Speech and Visual Form*. MIT Press, Cambridge, pp. 362–380.
- Borgefors, G., 1984. Distance transformations in arbitrary dimensions. *CVGIP* 27, 321–345.
- Bosl, W.J., Dvorkin, J., Nur, A., 1998. A study of porosity and permeability using a lattice Boltzmann simulation. *Geophys. Res. Lett.* 25, 1475–1478.
- Bryant, S.L., Mellor, D.W., Cade, C.A., 1993. Physical representative network models of transport in porous media. *AIChE J.* 39 (3), 387–396.
- Celia, M.A., Reeves, P.C., Ferrand, L.A., 1995. Recent advances in pore scale models for multiphase flow in porous media. *Rev. Geophys., Suppl.* (7), 1049–1057.
- Chen, S., Doolen, G.D., 1998. Lattice Boltzmann method for fluid flow. *Annu. Rev. Fluid Mech.* 30, 329–364.

- Chopard, B., Droz, M., 1998. *Cellular Automata Modeling of Physical Systems*. Cambridge Univ. Press, Cambridge.
- Coker, D.A., Torquato, S., Dunsmuir, J.H., 1996. Morphology and physical properties of Fontainebleau sandstone from tomographic analysis. *J. Geophys. Res.* 100, 17497–17506.
- Dahlstrom, D.A., Silverblatt, C.E., 1977. Continuous vacuum and pressure filtration. In: Purchas, D.B. (Ed.), *Solid Liquid Separation and Scale Up*. Up Lands Press, Croydon, pp. 445–491.
- Dardis, O., McCloskey, J., 1998. Permeability porosity relationships from numerical simulation of fluid flow. *Phys. Res. Lett.* 25, 1471–1474.
- Dullien, F.A.L., 1992. *Porous Media: Fluid Transport and Pore Structure*, 2nd ed. Academic Press, San Diego, CA.
- Ferreol, B., Rothman, D.H., 1995. Lattice-Boltzmann simulations of flow through Fontainebleau sandstone. *Transp. Porous Media* 20, 3–20.
- Frisch, U., Hasslacher, B., Pomean, Y., 1986. Lattice-gas automata for the Navier–Stokes equations. *Phys. Rev. Lett.* 56, 1505–1508.
- Furst, J.D., Pizer, S.M., Eberly, D.H., 1996. Marching cores: a method for extracting cores from 3D medical images. *Proc. Mathematical Methods in Biomedical Image Analysis*. IEEE Computer Society, San Francisco, CA, pp. 124–130.
- Gagvani, N., Silver, D., 1997. Parameter controlled skeletonization of three dimensional objects. Technical Report CAIP_TR_216, Rutgers University, June 1997, pp. 1–19.
- Gong, W.X., Bertrand, G., 1990. A simple parallel 3D thinning algorithm. *Int. Conf. Pattern Recognit.*, 188–190.
- Gunstensen, A.K., Rothman, D.H., 1993. Lattice-Boltzmann studies of two-phase flow through porous media. *J. Geol. Res.* 98, 6431–6441.
- Koponen, K., Kataja, M., Timonen, J., 1997. Permeability and effective porosity of porous media. *Phys. Rev.*, E 56, 3319–3325.
- Lee, T.C., Kashyap, R.L., Chu, C.N., 1994. Building skeleton models via 3-D medial surface/axis thinning algorithms. *CVGIP* 56, 462–478.
- Lin, C.L., Miller, J.D., 2000. Pore structure and network analysis of filter cake. *Chem. Eng. J.* 80, 221–231.
- Lin, C.L., Miller, J.D., 2001. A new cone beam X-ray microtomography facility for 3D analysis of multiphase materials. To be presented at 2nd World Congress on Industrial Process Tomography, Hannover, Germany, 29th–31st August.
- Lymberopoulos, D.P., Payatakes, A.C., 1992. Derivation of geometrical and correlation properties of porous media from pore chart analysis of serial section data. *J. Colloid Interface Sci.* 150 (1), 61–80.
- Ma, C.M., Sonka, M., 1996. A fully parallel 3D thinning algorithm and its applications. *Comput. Vis. Image Underst.* 64, 420–433.
- Maier, R.S., Kroll, D.M., Kutsovsky, Y.E., Davis, H.T., Bernard, R.S., 1998. Simulation of flow through bead packs using the lattice Boltzmann method. *Phys. Fluids* 10, 60–74.
- Martys, N., Chen, H., 1996. Simulation of multicomponent fluids in complex three-dimensional geometries by the lattice Boltzmann method. *Phys. Rev.*, E 53, 743–750.
- Martys, N.S., Torquato, S., Bentz, D.P., 1994. Universal scaling of fluid permeability for sphere packings. *Phys. Rev.*, E 50, 308–403.
- Noble, D.R., Chen, S., Georgiadis, J.C., Buckius, R., 1995. A consistent hydrodynamic boundary condition for the lattice Boltzmann method. *Phys. Fluids* 7 (1), 203–209.
- Ogniewicz, R., Ilg, M., 1992. Voronoi skeletons: theory and applications. *Proc. IEEE Conf. on Computer Vision and Pattern Recognition*, Champaign, Illinois, June. IEEE, NY, pp. 63–69.
- Qian, Y., D’Humières, D., Lallemand, P., 1992. Lattice BGK models for Navier–Stokes equations. *Europhys. Lett.* 17 (6), 479–484.
- Quiblier, J.A., 1984. A new three-dimensional modeling technique for studying porous media. *J. Colloid Interface Sci.* 98, 84–102.
- Rothman, D.H., Zaleski, S., 1997. *Lattice Gas Cellular Automata*. Cambridge Univ. Press, Cambridge.
- Sahimi, M., 1995. *Flow and Transport in Porous Media and Fractured Rock*. VCH, Weinheim.
- Stockman, H.W., 1999. A 3D lattice Boltzmann code for modeling flow an multi-component dispersion. Sandia Report SAND99-0162.
- Stockman, H.W., 2001. Private communications.
- Stockman, H.W., Cooper, C., Li, C., Perea-Reeves, S.J., 1997. Practical application of lattice-gas and lattice Boltzmann methods to dispersion problems. *International Journal Complex Systems*, paper 90. Available at <http://www.sandia.gov/eeseector/gsc/hws/saltfing.htm>.
- Stockman, H.W., Glass, R.J., Cooper, C., Rajaram, H., 1998. Accuracy and computational efficiency in 3D dispersion via lattice-Boltzmann models for dispersion in rough fractures and double-diffusion fingering. *Int. J. Mod. Phys. C* 9 (8), 1545–1557.
- Succi, S., Amati, G., Benzi, R., 1995. Challenges in lattice Boltzmann computing. *J. Stat. Phys.* 81, 5–16.
- Svarosvsky, L., 1990. Filtration fundamentals. In: Svarosvsky, L. (Ed.), *Solid–Liquid Separation*. Butterworth, London, pp. 311–337. Chapter 9.
- Thovet, J.-F., Salles, J., Adler, P.M., 1993. Computerized characterization of the geometry of real porous media: their discretization, analysis and interpretation. *J. Microsc.* 170, 65–79.
- Tiller, F.M., 1975. *Filtr. Sep.* 12, 386.
- Torquato, S., 1991. Random heterogeneous material: microstructure and improved bounds on effective properties. *Appl. Mech. Rev.* 44, 37–76.
- Tsao, Y.F., Fu, K.S., 1981. A parallel thinning algorithm for 3D pictures. *Comput. Graph. Image Process.* 17, 315–331.
- Wolf-Gladrow, D.A., 2000. *Lattice-Gas Cellular Automata and Lattice Boltzmann Models*. Springer, New York.
- Yao, J., Frykman, P., Kalaydjian, F., Thovet, J.-F., Adler, P.M., 1993. High-order moments of the phase function for real and reconstructed model porous media: a comparison. *J. Colloid Interface Sci.* 156, 478–490.
- Zick, A.A., Homsy, G.M., 1982. Stokes flow through periodic arrays of spheres. *J. Fluid Mech.* 115, 13–26.